PHYSICAL REVIEW APPLIED **23,** 054055 (2025)

Giant band gaps in a phononic crystal with touching solid inclusions

David Röhlig[*] and Angela Thränhardt
Institute of Physics, Chemnitz University of Technology, Reichenhainer Straße 70, 09126 Chemnitz, Germany

Vincent Laude[†]
Université Marie et Louis Pasteur, CNRS, FEMTO-ST Institute, 15B avenue des Montboucons,
25030 Besançon, France

Thomas Blaudeck
Fraunhofer Institute for Electronic Nano Systems (ENAS), Technologie-Campus 3, 09126 Chemnitz, Germany and
Research Center for Materials, Architectures and Integration of Nanomembranes (MAIN),
Chemnitz University of Technology, Rosenbergstraße 6, 09126 Chemnitz, Germany

(Received 18 December 2024; revised 13 February 2025; accepted 15 April 2025; published 21 May 2025)

We present a two-dimensional phononic crystal structure that exhibits exceptionally large complete band gaps, akin to those typically associated with bubble crystals. Our analysis begins with numerical simulations of a phononic crystal characterized by material parameters that are continuous functions of spatial coordinates, arriving at a sawtooth material parameter function, whose band structure can be replicated by a surprisingly simple configuration with inclusions touching at a single point, effectively functioning as a broadband filter. This allows us to perform acoustic frequency response measurements on a real system that confirm the sound isolation capabilities of our design, thereby underscoring its practical potential.

DOI: 10.1103/PhysRevApplied.23.054055

I. INTRODUCTION

Periodically arranged air bubbles in water are heralded as the prototype for achieving ultrawide sonic band gaps. They possess the largest complete band gaps ever reported among all known sonic and phononic crystals, both for two-dimensional [1] and for three-dimensional [2] configurations. Such a sonic crystal theoretically possesses the capability to inhibit the propagation of sound across an exceptionally wide and remarkably low frequency range.

More than two decades ago, Kushwaha *et al.* [1] illustrated this phenomenon for two-dimensional bubble sonic crystals, revealing that the widest band gaps are achieved at the lowest filling fractions. This observation naturally suggests that the extent of sonic band gaps in bubble crystals results from the hybridization of the propagating mode in the embedding water matrix with the collective Minnaert resonances of the air bubbles [3,4]. Discerning the exact mechanism of band formation from the band structures is challenging, as these structures predominantly exhibit very flat bands corresponding to the resonant modes intrinsic to the air bubble system [2,5]. The very low frequency ranges, which do not fall within the domain of conventional Bragg gaps, are of particular interest. The potential for a subwavelength band gap to emerge in bubble phononic crystals has been analytically and numerically demonstrated [6], revealing the potential for wave localization through the introduction of point defects [7] or line defects [8].

Although the theoretical framework for these structures is well developed, the practical realization of bubble crystals presents considerable challenges [9]. Leroy *et al.* [4] stated: “Generating stable equally sized bubbles arranged on a crystal lattice in water is not an easy, if not impossible, task.”

To circumvent fabrication difficulties, alternative matrix materials have frequently been explored. Specifically, transmission measurements were conducted on systems comprising air cavities of various shapes within a polymeric matrix, in contrast to the conventional spherical bubbles in water [4,10,11]. They revealed the presence a Bragg gap that is quite sensitive to positional disorder and a hybridization gap that survives it [4]. Additionally, triangular and square air cavities in polymers have been successfully three-dimensionally printed [12]. Huang *et al.* [13] succeeded in approximating a bubble crystal using a pillar-structured substrate to trap air bubbles and

---

[*] Contact author: david.roehlig@physik.tu-chemnitz.de
[†] Contact author: vincent.laude@femto-st.fr

Published by the American Physical Society under the terms of the Creative Commons Attribution 4.0 International license. Further distribution of this work must maintain attribution to the author(s) and the published article’s title, journal citation, and DOI.

form patterned single-layer and multilayer arrays. While the resulting structure does not exhibit an exceptionally wide band gap, it indeed possesses the anticipated low-frequency range. Nevertheless, it remains obvious that, despite amazing theoretical predictions indicating the presence of extensive band gaps, bubble crystals remain largely idealized constructs. This observation is particularly relevant to locally resonant crystals: while band gaps hold considerable promise in theory, they frequently turn out to be relatively narrow in practical scenarios [14–16].

Recently, a new type of phononic crystal has been proposed, featuring a spatial distribution of material properties, which are described by continuous parameter functions [17]. Remarkably, these structures exhibit broad complete band gaps similar to those that are typically associated with air bubbles in water. In this context, achieving significant sound isolation is not confined to the sensitive bubble system that is nearly impossible to fabricate. Instead, such band gaps could be effectively realized with functionally graded materials or gradient-index materials, which are already known for being capable of broadband absorption [18].

In this article, we elucidate the origins of such extensive band gaps and demonstrate that similar results can be achieved with an alternative, easily fabricated structure. Specifically, we used well-drawn wax candles, which exhibit a highly homogeneous density and minimal surface roughness. Owing to their widespread market availability and the ease with which they can be arranged adjacently on a flat surface, the candle structure provides—in opposition to bubble crystals—a convenient means of fabrication. We introduce an approach incorporating a theoretically infinitesimally thin wall. Despite its fundamental nature, this and similar structures have, to our knowledge, not been addressed in the existing literature. With this, we present an experimental realization of a two-dimensional phononic crystal, showcasing exceptionally large low-frequency band gaps, akin to those observed in bubble crystals.

II. NUMERICAL METHODS

A. Acoustic wave propagation

The propagation of acoustic waves in fluids—including liquids and gases—can be described by the following coupled first-order differential equations, which contain the pressure and velocity fields p and $\mathbf{v}$:

$$-\frac{1}{\rho(\mathbf{r})}\nabla p(\mathbf{r},t)=\frac{\partial \mathbf{v}(\mathbf{r},t)}{\partial t}, \tag{1}$$

$$\frac{1}{B(\mathbf{r})}\frac{\partial p(\mathbf{r},t)}{\partial t}=-\nabla\cdot\mathbf{v}(\mathbf{r},t), \tag{2}$$

where ρ denotes the mass density and B the bulk modulus [19]. These equations hold true for purely longitudinal displacements, ignoring viscoelasticity and external forces. Because of the sufficiently high material contrasts between the solid scatterers and the air matrix considered in this work, the transverse modes within the solids can be regarded as negligible—they remain localized and do not propagate [20]. Consequently, waves inside the solid scatterers are modeled in the following as pressure waves for all analyzed geometries, with the use of Eqs. (1) and (2). Apart from the case of complex band structures, it is common to simplify the governing equations by converting them into a scalar second-order differential equation, solely defined for pressure.

Given that all numerical methods considered in this work are based on the finite-element method (FEM), it is imperative to take account of the variational formulation. By multiplying the second-order pressure equation by the complex conjugate of the test function q, integrating over the different material domains Ω_i within the unit cell, and applying the divergence theorem, we derive the following expression:

$$\begin{aligned}0=&\int_{\Omega_i} q^*\frac{1}{B}\frac{\partial^2 p}{\partial t^2}\,\mathrm{d}\mathbf{r}+\int_{\Omega_i}\nabla q\cdot\left(\frac{1}{\rho}\nabla p\right)\mathrm{d}\mathbf{r}\\&-\int_{\sigma_i} q\left(\frac{1}{\rho}\nabla p\right)\cdot\mathbf{n}\,\mathrm{d}s\quad\text{for all } q.\end{aligned} \tag{3}$$

The final term represents a surface integral along the boundaries σ_i, incorporating the normal vector $\mathbf{n}$.

B. Real band structures

For the computation of the band structure, we start with Eq. (3) and simply apply periodic boundary conditions on each pair of external boundaries, thus eliminating the need for the integral over the boundaries σ_i. As we are interested only in Bloch wave propagation within an infinite periodic structure, we can specify our formulation by inserting monochromatic Bloch solutions $u(\mathbf{r},t)=\tilde{u}(\mathbf{r})\exp(i\omega t-i\mathbf{k}\cdot\mathbf{r})$ for both the pressure and the test function. This results in

$$\begin{aligned}&\omega^2\int_{\Omega_i}\tilde{q}^*\frac{1}{B}\tilde{p}\,\mathrm{d}\mathbf{r}\\&=\int_{\Omega_i}(\nabla\tilde{q}-i\mathbf{k}\tilde{q})^\dagger\frac{1}{\rho}(\nabla\tilde{p}-i\mathbf{k}\tilde{p})\,\mathrm{d}\mathbf{r}\quad\text{for all }\tilde{q}.\end{aligned} \tag{4}$$

If the material parameters are piecewise-defined functions with discontinuities at the boundaries between the inclusion and the matrix, the integrals can be decomposed over individual subdomains Ω_i. By varying the wave vector along a path in $\mathbf{k}$ space, we can now compute a set of eigenfrequencies.

C. Complex band structures

A method for deducing a complex eigenvalue problem in the form $k(\omega)$ involves initially reducing the wave vector $\mathbf{k}$ to an eigenvalue k with just a single degree of freedom [21–23]. This is achieved by one fixing it to a specific direction, delineated by a unit vector $\hat{\boldsymbol{\alpha}}$, which is selected on the basis of the path in $\mathbf{k}$ space. After substituting $\mathbf{k} = k\hat{\boldsymbol{\alpha}}$ into Eqs. (1) and (2) and labeling the acceleration in the propagation direction by $\Phi = i\omega\hat{\boldsymbol{\alpha}} \cdot \tilde{\mathbf{v}}$, we represent the solutions as a vector $(\tilde{p}, \Phi)$. Considering Bloch solutions once again, the variational form for the test functions $(\tilde{q}, \Psi)$ can be derived, resulting in

$$\int A(\Phi,\tilde{p};\,\Psi,\tilde{q})\ \mathrm{d}\mathbf{r} = (ik)\int B(\Phi,\tilde{p};\,\Psi,\tilde{q})\ \mathrm{d}\mathbf{r}\ \ \text{for all } (\Psi,\tilde{q}), \tag{5}$$

with

$$A(\Phi,\tilde{p};\,\Psi,\tilde{q}) = \Psi^*\Phi + \Psi^*\frac{1}{\rho}(\hat{\boldsymbol{\alpha}}\cdot\nabla\tilde{p}) + \omega^2\tilde{q}^*\frac{1}{B}\tilde{p} - (\nabla\tilde{q})^\dagger\frac{1}{\rho}\nabla\tilde{p}, \tag{6}$$

$$B(\Phi,\tilde{p};\,\Psi,\tilde{q}) = \Psi^*\frac{1}{\rho}\tilde{p} - (\hat{\boldsymbol{\alpha}}\cdot\nabla\tilde{q})^*\frac{1}{\rho}\tilde{p} - \tilde{q}^*\Phi. \tag{7}$$

Unlike with Eq. (4), we now encounter a generalized eigenvalue problem that is not Hermitian anymore.

D. Transmission

To investigate the transmission properties of our system, we revert to the variational formulation (3), with the addition of a source term. Therefore, the left-hand side of the equation is no longer zero but is instead

$$\int_{\sigma_1} q\left(\frac{1}{\rho}\nabla p\right)\cdot\mathbf{n}\ \mathrm{d}s. \tag{8}$$

This integral describes the normal acceleration of the fluid. By assigning a specific value at the boundary σ_1, as labeled in Fig. 5, we can introduce a source. For a plane wave where $\nabla p = -i\mathbf{k}p$, we can rewrite the integrand as follows:

$$q\left(\frac{1}{\rho}\nabla p\right)\cdot\mathbf{n} = -\frac{iqp}{\rho}\,\mathbf{k}\cdot\mathbf{n}. \tag{9}$$

We desire the waves to freely exit the simulation cell. An effective way to achieve this is by applying radiation boundary conditions. Thus, we set

$$\mathbf{k}\cdot\mathbf{n} = \frac{\omega}{c}, \tag{10}$$

with the sound velocity $c = \sqrt{B/\rho}$ inside the medium. The expression in Eq. (10) is used within the integrals over the boundaries σ_1 and σ_2. We define this condition for the propagation direction x, while we apply periodic boundary conditions for the y direction. To finally obtain the transmission for specific frequencies, we integrate over the external cell boundary σ_2, which is drawn on the right side in Fig. 5:

$$T = \frac{1}{a p_0}\int_{\sigma_2} p\ \mathrm{d}s, \tag{11}$$

with p_0 the initial pressure generated by the source, and a the length of the cell in the y direction—equivalent to a lattice constant.

For a more comprehensive understanding of the theoretical foundations outlined in this section, the reader is encouraged to consult Ref. [21].

III. SIMULATION RESULTS

To elucidate the origin of ultrawide complete band gaps in bubble-type phononic crystals, we begin by comparing three distinct unit cells of size $a \times a$ and their corresponding band structures for the square lattice. These three configurations are illustrated in Fig. 1.

We commence with a classical unit cell, featuring a circle with radius $R = a/4$. In this setting, the shape function $f(r)$ is defined as a piecewise-defined step function. The second configuration comprises the recently published

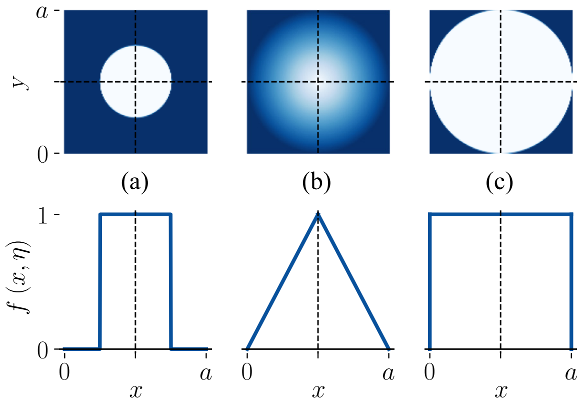

FIG. 1. The shape functions $f(x,\eta)$ in one dimension and $f(\sqrt{x^2+y^2},\eta)$ in two dimensions are depicted for three distinct crystal unit cells with area $a \times a$: (a) a sharp-edged circle with radius $R = a/4$ for $\eta \to 0$; (b) a crystal with a linear material transition; (c) another sharp-edged circle, this time with radius $R = a/2$ for $\eta \to 0$, making contact with the domain wall.

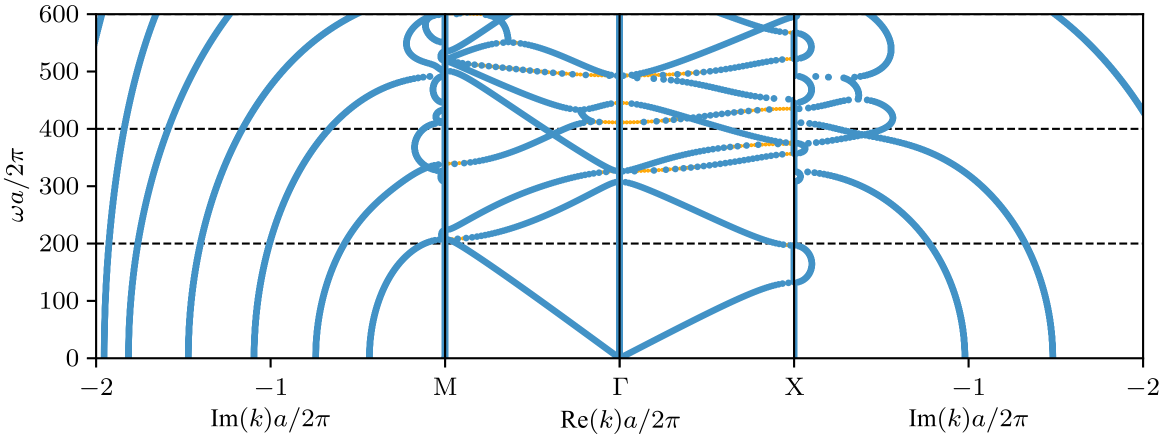

FIG. 2. Complex band structure for the system depicted in Fig. 1(a), comprising steel circles of radius $R = a/4$ embedded in air. The real solutions, situated at the center, are enclosed by the negative imaginary components of k. Additionally, for comparative purposes, the purely real band structure is superimposed in the real section, highlighted in orange.

function crystal, characterized by a seamless fusion of constituent material properties within the crystal lattice [17]. For this case, the structural function corresponds to

$$f(r,\eta) = \frac{\tanh\left(\frac{R-r}{\eta}\right) - \tanh\left(\frac{R-a/2}{\eta}\right)}{\tanh\left(\frac{R}{\eta}\right) - \tanh\left(\frac{R-a/2}{\eta}\right)}, \qquad (12)$$

with η being the broadening parameter. Within the range $r = \sqrt{x^2 - y^2} \in \mathbb{R} \in [0, a/2]$, this function varies between $f\,(a/2,\,\eta) = 0$ and $f\,(0,\,\eta) = 1$, as depicted in Fig. 1(b). This formulation not only encompasses the scenario of a linear material transition as $\eta \to \infty$ [as depicted in Fig. 1(b)] but also approximates conventional sharp-edged material transitions when $\eta \to 0$ [see Figs. 1(a) and 1(b)]. The material parameters ρ and B are simultaneously modulated by the shape function. For the density, this takes the form $\rho(r,\eta) = \rho_{\mathrm{M}} + f\,(r,\eta)(\rho_{\mathrm{S}} - \rho_{\mathrm{M}})$, where ρ_{S} denotes the value of the scatterer and ρ_{M} that of the matrix material; the same definition applies to the bulk modulus.

Lastly, we juxtapose these structures with a unit cell featuring a circle of radius $R = a/2$, as visualized in Fig. 1(c). Note that the circle touches the cell boundary at a single point, thereby creating a cavity of the matrix material, enclosed by the lattice inclusions. Representing this structure on a finite-element mesh poses challenges. Remarkably, despite the fundamental character of this issue, there appears to be no published work addressing a similar lattice where inclusions extend to make contact with the external boundary of the unit cell. To address the problem of constructing an appropriate mesh, the following procedure is proposed: The external boundaries must be subdivided precisely at the points where the inclusions intersect them. Furthermore, it is essential to delineate new domains accordingly. In the case illustrated in Fig. 1(c), this results in the creation of five distinct domains. Each one should be enclosed by a distinct boundary.

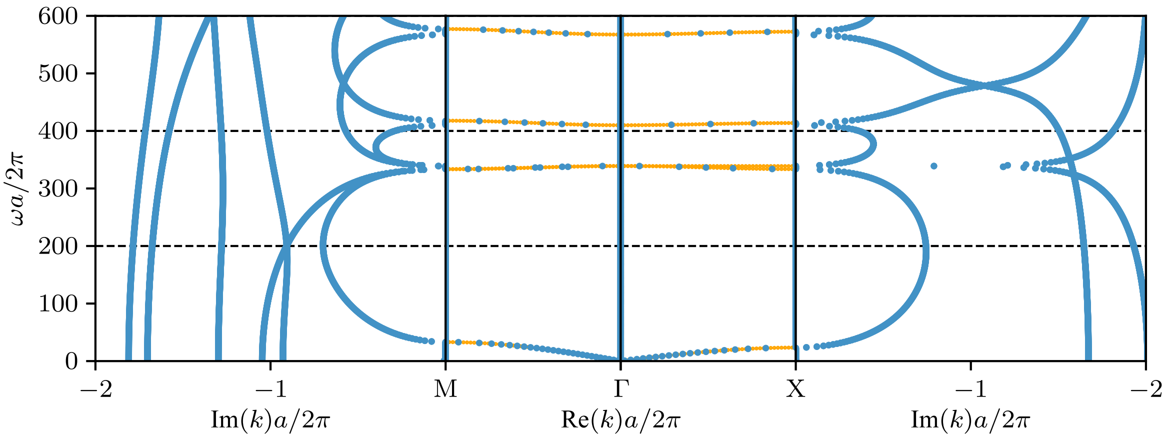

FIG. 3. Complex band structure, analogous to Fig. 2, for the system characterized by the function $f(\mathbf{r}, \eta \to \infty)$, as depicted in Fig. 1(b). The material parameters undergo a linear transition between the values representative of steel and air.

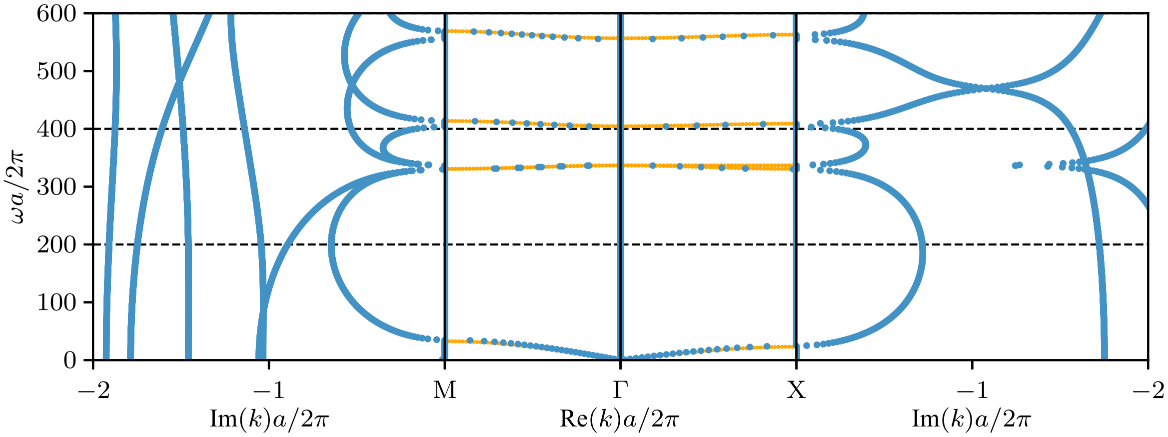

FIG. 4. Complex band structure, analogous to Fig. 2, for the system illustrated in Fig. 1(c). This configuration consists of contiguous steel circles with radius $R = a/2$ embedded in air.

A. Band structures

We now present the relationships between the band structures of the three distinct unit cells. Figures 2–4 show the complex band structures, which are the solutions of Eq. (5). These were computed with the use of a mesh composed of elements defined by second-degree polynomials, with a resolution of 30 triangular nodes per lattice constant a. Regarding material parameters, we used rigid circles made of steel with density $\rho_S = 7860$ kg/m^3 and bulk modulus $B_S = 160$ GPa. These are embedded within an air matrix, which has density $\rho_A = 1.2$ kg/m^3 and bulk modulus $B_A = 142$ kPa. Centrally in Figs. 2–4, the real part of k is displayed along the paths from Γ to X and Γ to M including the symmetry points $\Gamma = (0,0)^T$, $X = (\pi/a, 0)^T$, and $M = (\pi/a, \pi/a)^T$. For a more comprehensive analysis, we also show the solutions of Eq. (4), representing the purely real band structure. The real solutions (in the center in Figs. 2–4) are enclosed by the negative imaginary part of k for the same two paths in reciprocal space—on the left and right sides in Figs. 2–4.

We start our analysis with the case illustrated in Fig. 1(a) of circles with radius $R = a/4$, depicted in Fig. 2, where no complete band gap is observed. However, some partial band gaps become apparent, particularly through evanescent arclike branches that continuously connect bands with their foldings at the symmetry points. These features are typical indicators of Bragg gaps [21]. Additionally, numerous purely evanescent branches are visible—each with a distinct frequency cutoff. One example is the first band (starting from zero) in the imaginary part corresponding to the M point. This band has its cutoff at a frequency of approximately 200 m/s. The vertical blue lines at the high-symmetry points within the center panel in Fig. 2 exclusively represent the real part of complex Bloch wave numbers whose imaginary part is varying.

When using the linear function $f(\mathbf{r}, \eta \to \infty)$, we witness a profoundly altered band structure, as seen in Fig. 3. In the real part, the bands are significantly flatter, resulting in exceptionally wide complete band gaps. In the imaginary part, the purely evanescent branches become arc circles, with their midpoints located where the frequency cutoffs were previously observed. Interestingly, the distribution of eigenvalues—particularly in the real part—exhibits a striking resemblance to distribution associated with the well-known bubble crystal.

We now arrive at a particularly intriguing scenario: Consider a circle with radius $R = a/2$, in contact with the domain wall. Surprisingly, the band structure calculated for this case, as shown in Fig. 4, remains almost identical to the previous result, characterized by complete frequency gaps. A comparison with Fig. 3 reveals that as we increase the broadening parameter η in Eq. (12), we effectively achieve convergence toward the band structure of the simple touching-cylinder system. This is evident for the real part and nearly so for the imaginary part.

Even though the structures corresponding to Figs. 1(b) and 1(c) differ from the two-dimensional bubble crystal in their material configuration, the flat-band characteristics paired with ultrawide frequency gaps render them comparable. In the bubble crystal, flat bands are attributed to the resonant behavior of the bubbles [3,4]. By contrast, the band structures corresponding to the cases in Figs. 1(b) and 1(c) exhibit no clear indications of resonance effects; instead, they suggest the predominance of the Bragg mechanism. When one compares the cases in Figs. 1(b) and 1(c), it becomes apparent that the pronounced similarity between these configurations is primarily attributable not to the circles themselves but rather to their contact points.

Figure 5 illustrates a simulation cell, for the transmission calculation, which will be detailed shortly. It showcases both the pressure field and the Poynting vector for the mode at a reduced frequency of 405 m/s (situated on the third band in Fig. 4). It is evident that the pressure reaches its maximum values at the touching points between

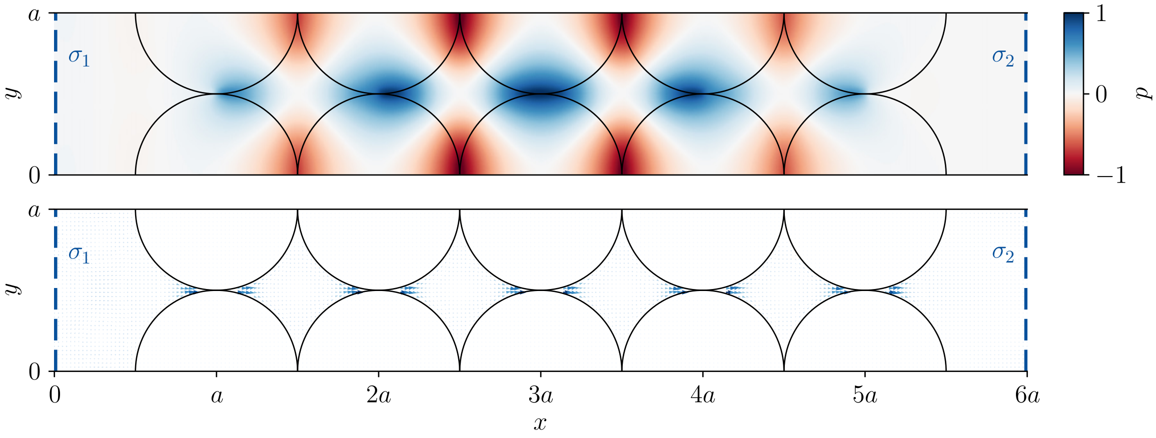

FIG. 5. Distribution of both the normalized pressure (top) and the Poynting vector (bottom) for a reduced frequency of 405 m/s, corresponding to the third band of the real part presented in Fig. 4. This was calculated for the arrangement of adjacent cylinders pictured in Fig. 1(c), with periodic boundary conditions applied in the y direction. This simulation cell was conceived to compute the one-dimensional transmission curves presented in Fig. 7. The source is defined at the boundary σ_1 (at $x = 0$), while the transmission is determined at σ_2 (at $x = 6a$).

the rigid circles. Additionally, the Poynting vector associated with this mode is predominantly and consistently concentrated at these contact points along the propagation direction. Such an energy pattern is not only characteristic of this specific mode but is observed across all analyzed cases. Additional calculations involving slightly overlapping circles, nearly touching circles, and alternative lattice configurations confirm that the system remains robust even under perturbations.

Overall, the numerical predictions suggest that the touching-circle system—owing to its giant band gaps—could be a viable candidate for effective sound isolation. Moreover, the flat-band characteristics imply that within the structure the group velocity is significantly reduced compared with the speed of sound in air. The highest velocity occurs at frequencies for which the crystal appears as a homogeneous medium—in the homogenization limit [24]. While for the conventional system as illustrated in Fig. 1(a), the effective velocity remains at around 315 m/s, it is drastically reduced to around 73 m/s for the case depicted in Fig. 1(b) and around 77 m/s for the case visualized in Fig. 1(c).

IV. EXPERIMENTAL RESULTS

For the experimental verification of the acoustic properties of the proposed structure, a simple setup comprising a model scatterer, a sound source, and a detector positioned on a table was conceived. To approximate the two-dimensional circular case, we chose elongated cylinders with a spherical base as solid inclusions of the crystal, which is commonly treated as a two-dimensional crystal in the literature [25]. Specifically, we selected wax candles (type *Stumpenkerze*, Gala, Ansbach, Germany), made from pure paraffin with density $\rho_S = 893$ kg/m^3. The candles, each with a height of 29 cm and radius $R = 4$ cm, were arranged in a 7×7 array, as pictured in Fig. 6. The form-fitting properties of the paraffin allowed the formation of a straight contact line for adjacent cylinders when they are touching one another, corresponding to a lattice constant $a = 2R$. Acoustic measurements were performed in a sound-attenuated room under ambient conditions. As a sound source, we used a loudspeaker (model Road-Buddy 10, LD Systems, Neu-Anspach, Germany) which we subjected to the emission of pulses defined as

$$g(t) = e^{-\frac{(t-t_0)^2}{2\sigma^2}} \cos(\omega_c t), \tag{13}$$

where $\sigma = 1/20\,000$ s, $\omega_c = 2\pi \times 4500$ Hz, and $t_0 = 0.05$ s, in accordance with the short-pulse excitation

FIG. 6. Photograph of an experimental realization of a two-dimensional phononic crystal structure, consisting of a 7×7 array of touching paraffin wax candles with radius $R = 4$ cm.

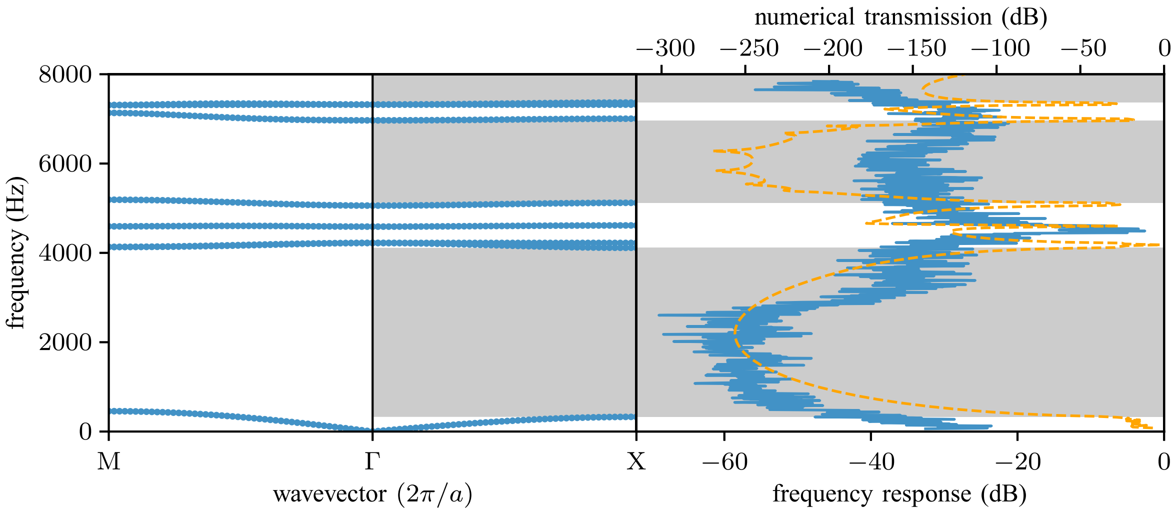

FIG. 7. Real band structure for the system depicted in Fig. 1(c) and pictured in Fig. 6, comprising touching paraffin circles of radius $R = 4$ cm embedded in air, on the left, compared with the frequency response measurement (blue curve) and the FEM transmission calculation (highlighted in orange), performed under radiation boundary conditions and periodic boundary conditions in the y direction.

method. A microphone as a point detector built in a cell phone (model iPhone 13, Apple Inc., Cupertino, USA) was positioned directly behind the structure, with both the source and the detector placed at a distance of 1 cm from the candle arrangement. The frequency response in terms of a sound spectrum was determined by means of the Fourier transformation of the recorded audio track that consists of 50 pulses. To normalize the spectrum, a reference measurement was performed under identical conditions but without the presence of the candle structure.

The results shown in Fig. 7, spanning the frequency range from 0 to 8000 Hz, reveal that the phenomena observed for touching cylinders are not limited to systems with high material contrasts. In the numerical simulation, we used a Poisson's ratio ν_S of 0.37 and an elastic modulus E_S of 116.3 MPa for the paraffin candles. From these parameters the bulk modulus B_S was calculated [see Eq. (4)]. As described in Sec. II A, we proceeded on the premise that pressure waves propagating in air do not impart substantial transverse motion within the solid medium.

Notably, even for wax candles embedded in air, flat bands emerge in the real band structure alongside wide frequency gaps. As a consequence, sound propagation within the candle structure is drastically slowed down, with an effective velocity of merely 13 m/s in the low-frequency limit. A comparison with frequency response measurements in the Γ-X direction confirms the numerical predictions: the amplitude decreases markedly within the band gap regions, while distinct maxima are observed near the bands.

Moreover, the one-dimensional FEM computations of transmission curves under radiation boundary conditions, depicted in Fig. 7, align closely with the experimental results. As previously mentioned, the simulation cell was based on the configuration in Fig. 5, adjusted to a resolution of 20 points per lattice constant, and extended to include seven rows to match the experimental scenario. Since the simulation assumes periodic boundary conditions in the y direction and is evaluated along the boundary σ_2, whereas the experiment involves a finite structure and a pointlike sensor, the amplitudes differ accordingly. Apart from this deviation, the results not only exhibit excellent agreement with the band structure but also support the experimental data. These findings underscore that the system acts as a highly effective frequency filter within the investigated range, consistent with the expected behavior of a bubble crystal.

V. CONCLUDING REMARKS

In summary, through both numerical analysis and experimental validation we have demonstrated that giant complete band gaps are indeed attainable from phononic crystals with a by far simpler system than the largely idealized construct of bubble crystals.

The investigation of a shape function, which manipulates material parameters, intriguingly converged upon a configuration consisting of mutually touching cylinders. This system is capable of concentrating states within narrow frequency bands characterized by notably low group velocities, thereby giving rise to remarkably large complete band gaps. Fortunately, this outcome is not restricted to complex geometries; rather, it can be replicated with a simple arrangement of wax candles touching each other linearly at their outer surfaces. Through acoustic measurements, we have demonstrated the practical efficacy of the system as a reliable frequency filter.

ACKNOWLEDGMENTS

This work was partially funded by a Ph.D. scholarship awarded by the Free State of Saxony (D.R.). Support by the TUCculture2025 initiative of Chemnitz University of Technology, the EIPHI Graduate School (Contract No. ANR-17-EURE-0002), and the Bourgogne-Franche-Comté Region is acknowledged. We also thank Alexandra Bendixen and Thomas Baumann for giving us the opportunity to conduct preliminary measurements in their sound-attenuated laboratory.

DATA AVAILABILITY

Data that support the findings of this article are openly available [26]. Further data is provided from the authors upon reasonable request.

[1] M. S. Kushwaha and B. Djafari-Rouhani, Giant sonic stop bands in two-dimensional periodic system of fluids, J. Appl. Phys. **84**, 4677 (1998).

[2] M. Kushwaha, B. Djafari-Rouhani, and L. Dobrzynski, Sound isolation from cubic arrays of air bubbles in water, Phys. Lett. A **248**, 252 (1998).

[3] R. Jerez Boudesseul and E. van 't Wout, Modeling frequency shifts of collective bubble resonances with the boundary element method, J. Acoust. Soc. Am. **153**, 1898 (2023).

[4] V. Leroy, A. Bretagne, M. Lanoy, and A. Tourin, Band gaps in bubble phononic crystals, AIP Adv. **6**, 121604 (2016).

[5] C. Goffaux and J. Vigneron, Spatial trapping of acoustic waves in bubbly liquids, Phys. B: Condens. Matter **296**, 195 (2001).

[6] H. Ammari, B. Fitzpatrick, H. Lee, S. Yu, and H. Zhang, Subwavelength phononic bandgap opening in bubbly media, J. Differ. Equ. **263**, 5610 (2017).

[7] H. Ammari, B. Fitzpatrick, E. O. Hiltunen, and S. Yu, Subwavelength localized modes for acoustic waves in bubbly crystals with a defect, SIAM J. Appl. Math. **78**, 3316 (2018).

[8] H. Ammari, E. O. Hiltunen, and S. Yu, Subwavelength guided modes for acoustic waves in bubbly crystals with a line defect, J. Eur. Math. Soc. **24**, 2279 (2021).

[9] D. Rabaud, P. Thibault, M. Mathieu, and P. Marmottant, Acoustically bound microfluidic bubble crystals, Phys. Rev. Lett. **106**, 134501 (2011).

[10] C. Horvath, Y. Vargas-Hernández, and M. L. Cordero, Minnaert resonance in an array of two-dimensional bubbles, Phys. Rev. Appl. **20**, 044007 (2023).

[11] V. Leroy, A. Bretagne, M. Fink, H. Willaime, P. Tabeling, and A. Tourin, Design and characterization of bubble phononic crystals, Appl. Phys. Lett. **95**, 171904 (2009).

[12] W. Gao, Y. Hou, F. Shang, and J. Zhang, 3D printed structures for ultrasound attenuation in underwater environment, 3D Printing and Additive Manufacturing **11**, 115 (2024).

[13] Z. Huang, S. Zhao, M. Su, Q. Yang, Z. Li, Z. Cai, H. Zhao, X. Hu, H. Zhou, F. Li, J. Yang, Y. Wang, and Y. Song, Bioinspired patterned bubbles for broad and low-frequency acoustic blocking, ACS Appl. Mater. Interfaces **12**, 1757 (2020).

[14] G. Ma and P. Sheng, Acoustic metamaterials: From local resonances to broad horizons, Sci. Adv. **2**, e1501595 (2016).

[15] K. H. Matlack, A. Bauhofer, S. Krödel, A. Palermo, and C. Daraio, Composite 3D-printed metastructures for low-frequency and broadband vibration absorption, Proc. Natl. Acad. Sci. USA **113**, 8386 (2016).

[16] J. Mei, G. Ma, M. Yang, Z. Yang, W. Wen, and P. Sheng, Dark acoustic metamaterials as super absorbers for low-frequency sound, Nat. Commun. **3**, 756 (2012).

[17] D. Röhlig, E. Kuhn, F. Teichert, A. Thränhardt, and T. Blaudeck, Function phononic crystals, Europhys. Lett. **145**, 26001 (2024).

[18] X. Pan, X. Fang, X. Yin, Y. Li, Y. Pan, and Y. Jin, Gradient index metamaterials for broadband underwater sound absorption, APL Mater. **12**, 031111 (2024).

[19] L. Kinsler, A. Frey, A. Coppens, and J. Sanders, *Fundamentals of Acoustics* (Wiley, Hoboken, New Jersey, 2000), https://www.wiley.com/en-sg/Fundamentals+of+Acoustics.

[20] M. Kafesaki and E. N. Economou, Multiple-scattering theory for three-dimensional periodic acoustic composites, Phys. Rev. B **60**, 11993 (1999).

[21] V. Laude, *Phononic Crystals* (De Gruyter, Berlin, Boston, 2020).

[22] V. Laude, Y. Achaoui, S. Benchabane, and A. Khelif, Evanescent Bloch waves and the complex band structure of phononic crystals, Phys. Rev. B-Condens. Matter Mater. Phys. **80**, 092301 (2009).

[23] V. Romero-García, J. V. Sánchez-Pérez, S. Castiñeira-Ibáñez, and L. Garcia-Raffi, Evidences of evanescent Bloch waves in phononic crystals, Appl. Phys. Lett. **96**, 124102 (2010).

[24] V. Laude, J. A. Iglesias Martínez, Y.-F. Wang, and M. Kadic, Effective anisotropy of periodic acoustic and elastic composites, J. Appl. Phys. **129**, 215106 (2021).

[25] A. Khelif, A. Choujaa, B. Djafari-Rouhani, M. Wilm, S. Ballandras, and V. Laude, Trapping and guiding of acoustic waves by defect modes in a full-band-gap ultrasonic crystal, Phys. Rev. B **68**, 214301 (2003).

[26] https://doi.org/10.5281/zenodo.15348271.